ON THE IMPACT PROPERTIES AND FRACTURE MECHANISMS OF A356.2-TYPE CAST ALLOYS

A. M. Samuel and F. H. Samuel
Département des Sciences appliquées, Université du Québec à Chicoutimi, Chicoutimi, QC, Canada

H. W. Doty
General Motors Materials Engineering, Pontiac, MI, USA

S. Valtierra
Nemak, S.A., Garza Garcia, N.L., Mexico

Abstract

A study was carried out to investigate the effects of iron content, porosity and solidification rate on the impact properties and fracture behavior of A356.2-type alloys. The results show that impact properties improve with increase in solidification rate and decrease in Fe content. Unmodified A356.2 alloys show linear correlations, while modified A356.2 alloys show logarithmic correlations at all solidification rates ($R^2 > 0.95$ in all cases). Impact properties obtained at the highest solidification rate are far superior to those obtained at other solidification rates. The β-Al_5FeSi intermetallic deteriorates impact properties significantly, the effect being most apparent within 10–50 µm β-platelet sizes in A356.2 alloy. Fairly good correlations between porosity and impact properties are obtained. Strontium is effective in improving impact energy, even at high Fe levels. A good inverse relation is obtained between average crack speed and impact energy, highest crack speeds being observed in unmodified samples obtained at highest Fe contents and lowest solidification rates. Impact testing is sensitive to variations in microstructure or casting defects. Impact energy–strength plots show exponential relationships, whereas impact energy–ductility plots display linear relationships for all alloys, modified or not, regardless of the alloy composition. In A356.2 alloys, cracks initiate mainly through the fracture of Si particles or their debonding from the Al matrix, while crack propagation occurs through the coalescence of fractured Si particles, except when β-Al_5FeSi platelets are present, in which case the latter take precedence.

Keywords: *Al–Si–Mg alloys, impact toughness, tensile data, fractography, secondary cracking, intermetallics, porosity, modification*

Introduction

Many researchers have investigated the effect of iron on the mechanical properties of Al–Si alloys. In their review on iron in aluminum casting alloys, Ma et al.[1] reported that the addition of iron to aluminum–silicon alloys is detrimental to the mechanical properties. Increasing the iron content from 0.5 to 1.2% in an Al–13% Si casting alloy dramatically reduces the mechanical properties, particularly the ductility, due to the formation of β-Al_5FeSi phase platelets.[2]

Taylor[3] claimed that even a small Fe addition to Al–Si alloys seriously diminishes tensile strength and ductility, due to the formation of the brittle β-Al_5FeSi intermetallic phase at solidification rates normally employed in sand and permanent mold castings (about 0.9 °C/s in sand castings and 10 °C/s in permanent mold castings). The hard, brittle β-Al_5FeSi platelets have relatively low bond strength with the matrix.[4–8]

With regard to the effect of iron content on the mechanical properties of A356 type alloys, Nishi and Kobayashi[9] showed that the mechanical properties of Al–Si–Mg–Zn alloys were further deteriorated with the increase in iron content, and it was desirable to keep the iron content lower than 0.15%. Moustafa et al.[10] however found that iron in the range of 0.09–0.58% had little effect on the aging

characteristics of A413.1 alloys: increasing the Fe content lowered the ductility, with marginal effects on yield strength and hardness. To date, there are many investigations that are reported in the literature. Hafiz et al.[11] carried out a study on the relation between microstructure and fracture behavior in Al–Si casting alloys. They found that at the very beginning, the voids are generally initiated at silicon particles. The individual voids then grow and coalesce, creating microcracks in the eutectic region. These microcracks link up to form the main crack and then the final fracture.

Dighe and Gokhale[12] observed that in Al–Si–Mg cast alloys, the fracture path goes through fractured silicon particles, debonded silicon particles and the aluminum matrix. Failure occurs mainly because of the gradual debonding and fracture of silicon particles, followed by interlinkage of these damaged silicon particles through cracks that ultimately cause the fracture. Ibrahim et al.[13] pointed out that in A356 alloys, crack initiation or propagation is preceded by fracture of the silicon particles at relatively low values of strain. Further straining causes selected microcracks to link up with other neighboring microcracks in the same eutectic region to initiate the primary crack, or to link up with the propagating crack front. Fracture paths tend to follow the eutectic regions in the microstructure and avoid the pro-eutectic α-Al regions.

In the present work, A356.2 alloy was selected to study the effect of iron intermetallics on the impact properties to obtain an estimation of the scatter in properties expected with the use of industrial alloys. In order to emphasize certain aspects, the results were compared with those reported on the impact toughness of 319 alloys.[14]

Experimental Procedure

The primary A356.2 alloy used in this study was supplied in the form of 12.5-kg ingots. The chemical composition of the as-received alloy is listed in Table 1. In all cases, the melts were degassed using pure, dry argon, i.e., the hydrogen level was kept to a minimum, at ∼0.1 mL/100 g Al (where an AlScan™ apparatus was used to monitor the hydrogen level). Degassing was done using a rotary impeller (30 min at 150 rpm). Strontium additions of 200–250 ppm were made to the degassed melts, to compare modified and unmodified structures. Also, Al–5% Ti–1% B master alloy

was added to all the melts, for grain refining purposes. The Fe additions were made using Al–25% Fe master alloy in the required amounts. To promote iron dissolution (especially at high iron levels), the melt temperature was kept at ∼80–100 °C above the respective alloy melting point. Castings were done in a rectangular end-chilled mold, as shown in Figure 1. The four walls of the mold are made of refractory material to ensure proper thermal insulation, while the bottom is a water-chilled copper base, to promote directional solidification.

Using this mold arrangement, casting blocks were produced that exhibited a range of dendrite arm spacings (DASs, measured using the line intercept method) along the length of the casting, corresponding to solidification rates that decreased with increasing distance from the chill end. Table 2 indicates the average DASs that were obtained for the A356.2 alloy, corresponding to different distances from the chill end. For each pouring/casting, samplings for chemical analysis were also taken, to determine the exact composition of the melt. Chemical analyses were carried out at General Motors facilities in Warren, MI.

Impact energy values depend strongly on the testing method used. In the present study, Charpy unnotched simple beam impact samples were used, since the Charpy test is the most common laboratory method for the measurement of impact energy. The specimens were machined in accordance with ASTM E23 standards; the specimen dimensions are shown in Figure 2. Four such samples were obtained from each of the four 20-mm-thick specimen blanks sectioned per casting. Thus, four impact test specimens were obtained for each melt condition and level above the chill end. Prior to testing, the samples were T6 heat-treated which comprised solution heat treatment for 8 h at 540 °C, then quenched in warm water (60 °C), followed by artificial aging for 5 h at 155 °C. The scanning electron microscope (SEM) operated at 15 kV. In certain cases, samples were sectioned beneath the fracture surface for metallographic examination.

Results and Discussion

Impact Testing

Figure 3a shows the microstructure of an unmodified A356.2 alloy sample containing 0.1% iron (lowest level)

Table 1. Chemical Compositions of 356 Alloy

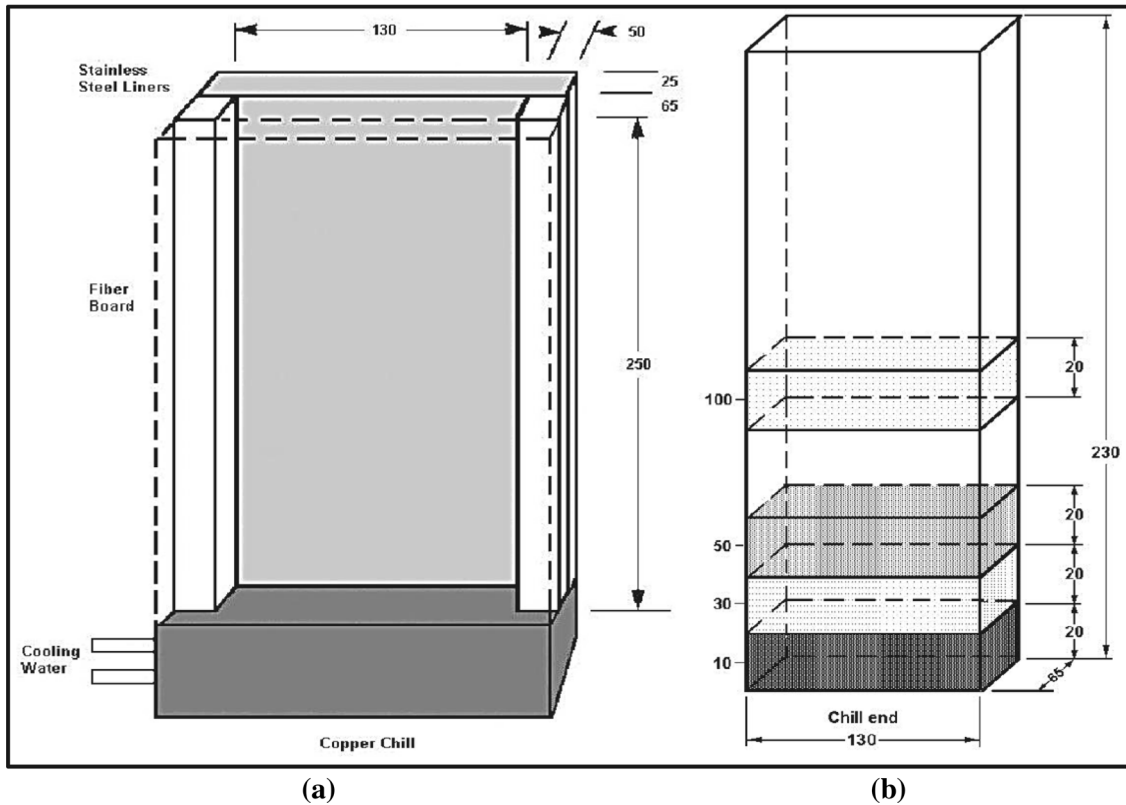| Alloy code	AA alloy	Elements (wt%)									
		Si	Cu	Mg	Fe	Mn	Zn	Ti	Sr	Pb	Al
IC	A356.2	6.78	0.02	0.33	0.11	0.04	0.04	0.08	–	0.03	Bal.

Figure 1. *(a) End-chill mold scheme, (b) end-chill casting showing specimen blank sectioning scheme.*

Table 2. DAS Values Obtained at Various Levels of the End-Chilled Castings for the A356.2 Alloys Used

Level	Distance from chill end (mm)	DAS (μm)
1	10	23
3	30	39
5	50	53
10	100	75

and obtained at the highest solidification rate. The main phases observed here are the aluminum dendrites and the eutectic Si particles. Due to the purity of the alloy (even if it is industrial) and the maximum solidification rate employed, the presence of other phases, including Mg_2Si, is negligible. The microstructure of an unmodified A356.2 alloy sample containing 0.6 wt% iron and obtained at the lowest solidification rate is shown in Figure 3b. Compared to the previous micrograph, all the microconstituents, including the grain size of the aluminum matrix, are much bigger. The large, acicular Si particles are distributed along the aluminum interdendritic boundaries; some are precipitated along the β-iron intermetallic platelets, observed as long needles all over the matrix. Their detrimental effect on the mechanical properties, particularly ductility, would explain why this alloy exhibits the lowest ductility and tensile strength (lowest quality index).[13] Some black Mg_2Si
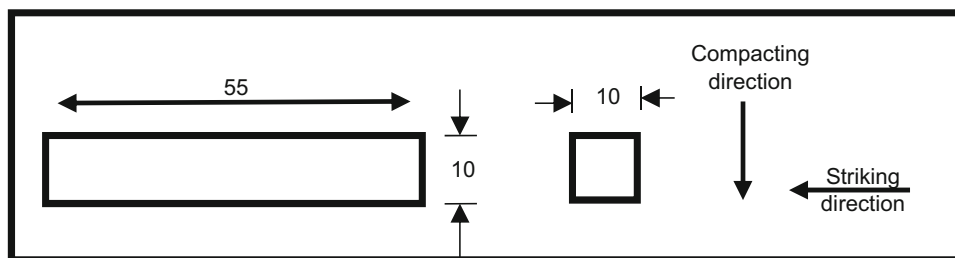

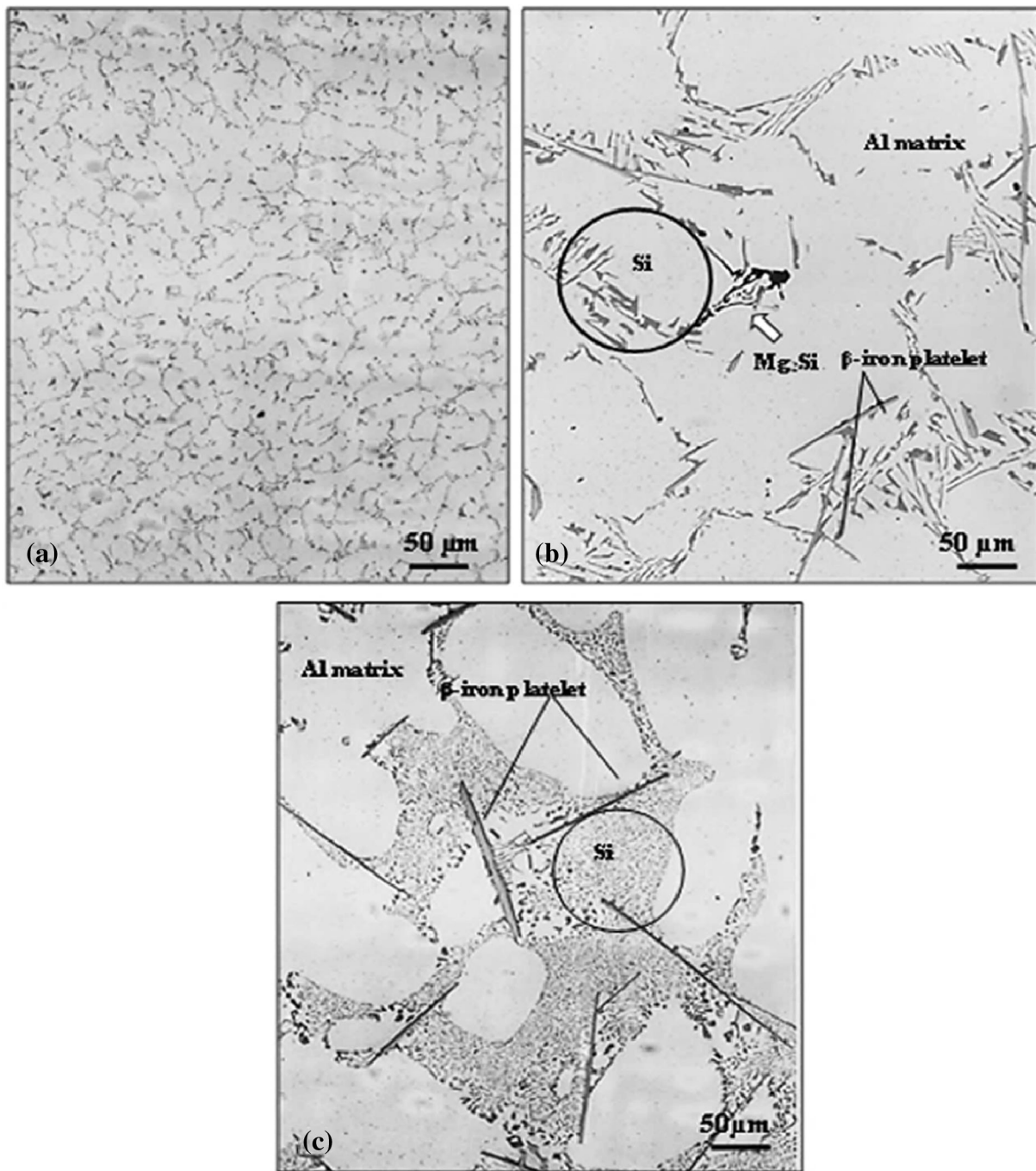**Figure 2.** *Charpy unnotched simple beam impact test specimen (all dimensions in mm).*

Figure 3. Optical microstructures of A356.2 alloy samples: (a) 0.1% Fe, DAS 23 μm, unmodified, (b) 0.6% Fe, DAS 75 μm and (c) 0.6% Fe, DAS 75 μm, Sr-modified.

Chinese script particles are also observed (arrowed), due to the sufficient solidification time for their precipitation.

The microstructure of the modified A356.2 alloy sample containing 0.6 wt% (highest) iron content and obtained at the lowest solidification rate is shown in Figure 3c. Compared to the unmodified condition, the most important feature is the change in morphology of the eutectic Si particles, from acicular to fully fibrous, which significantly increases the alloy properties. Long-sized β-platelets can

still be observed. Although their sizes did not seem to decrease very much from the unmodified to the modified condition, transformation from β-Al_5FeSi to α-$Al_8Mg_{3-}FeSi_6$ could be observed in certain cases.[13]

It should be mentioned here that in Figures 4, 5, 6 and 7, the IC in the legend refers to the unmodified A356.2 alloy, while ICS refers to the modified alloy. The impact energy data obtained from the A356.2 alloys are summarized in Table 3. The corresponding data distribution with respect
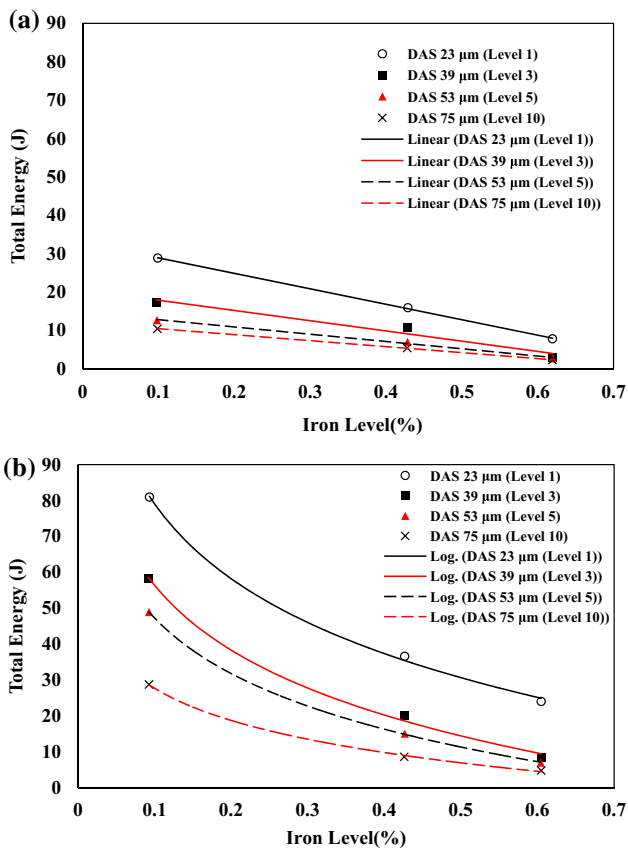
Figure 4. Total energy versus solidification rate and iron content in: (a) unmodified and (b) Sr-modified A356.2 alloys.

Figure 5. Total energy versus β-platelet size in the present alloys: (a) average maximum length and (b) average maximum area. Note that the values reported in (a) and (b) are based on 2D metallographic samples.

to solidification rate and iron content are plotted in Figure 4. Figure 4a shows that, for the unmodified A356.2 alloy, the impact energies depict linear relations versus Fe content at all solidification rates. Unlike the more complex 319 alloys, the impact energy in this Al–Si–Mg alloy is determined mainly by the eutectic Si particle characteristics at each solidification rate. However, in comparison with the 319.2 alloy, the corresponding impact energies at each DAS for a particular Fe level are always higher in the A356.2 alloy at every DAS level. At very low Fe levels, of the order of 0.1%, and at 23 μm DAS, the impact energy is ~29 J.[5]

Looking at the Fe contents, the impact energy is most sensitive to the Fe content at the lowest DAS. As the microstructure coarsens, the microconstituents therein also increase in size correspondingly, so that at the coarsest DAS, not much change in impact energy is observed with respect to the Fe level. Apparently, the intermetallics have already attained large enough sizes to lower the impact properties to a minimum. When the A356.2 alloy is modified with Sr, Figure 3b, significant improvements in impact energy are observed, particularly at the smallest DAS level. At the lowest Fe content, the impact energy is 81 J. In this case, the relationships are logarithmic in nature. Thus, a high solidification rate and Sr modification can improve the impact
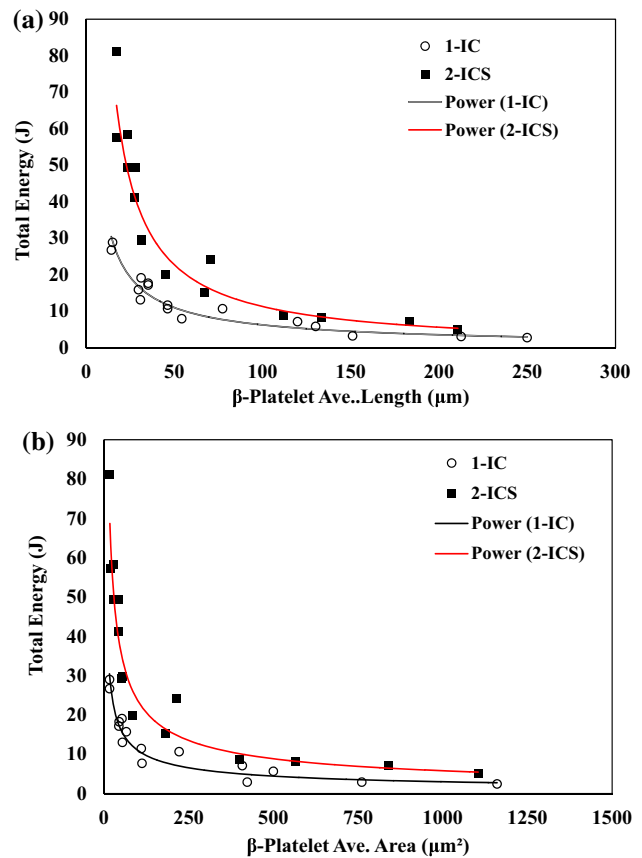
energy at high Fe levels considerably, to levels close to those observed in the unmodified alloy at the lowest DAS-lowest Fe level condition. Addition of Sr is also seen to separate the Fe and DAS levels from one another, even at their highest values. It is important to mention here that, as these β-platelets are actually three-dimensional entities, it is difficult to estimate correctly the actual volume fraction of the β-Al_5FeSi phase in the microstructure.

Optical micrographs only provide a two-dimensional picture from which we can at best estimate the area fraction of the phase by measuring the length and thickness of the needlelike β-platelets observed in such micrographs. Although, for purposes of quantitative metallography, area fractions are taken as equivalent to the volume fractions, the third dimension of these platelets can possibly have a critical effect on the feedability of the liquid metal during solidification, as well as the tortuosity of the crack propagation path during fracture, effects that cannot be incorporated in the property versus β-platelet size plots. This aspect should be kept in mind when analyzing the results.

The effect of the β-iron intermetallic size on the impact energy in the A356.2 alloy is shown in Figure 5. Note the
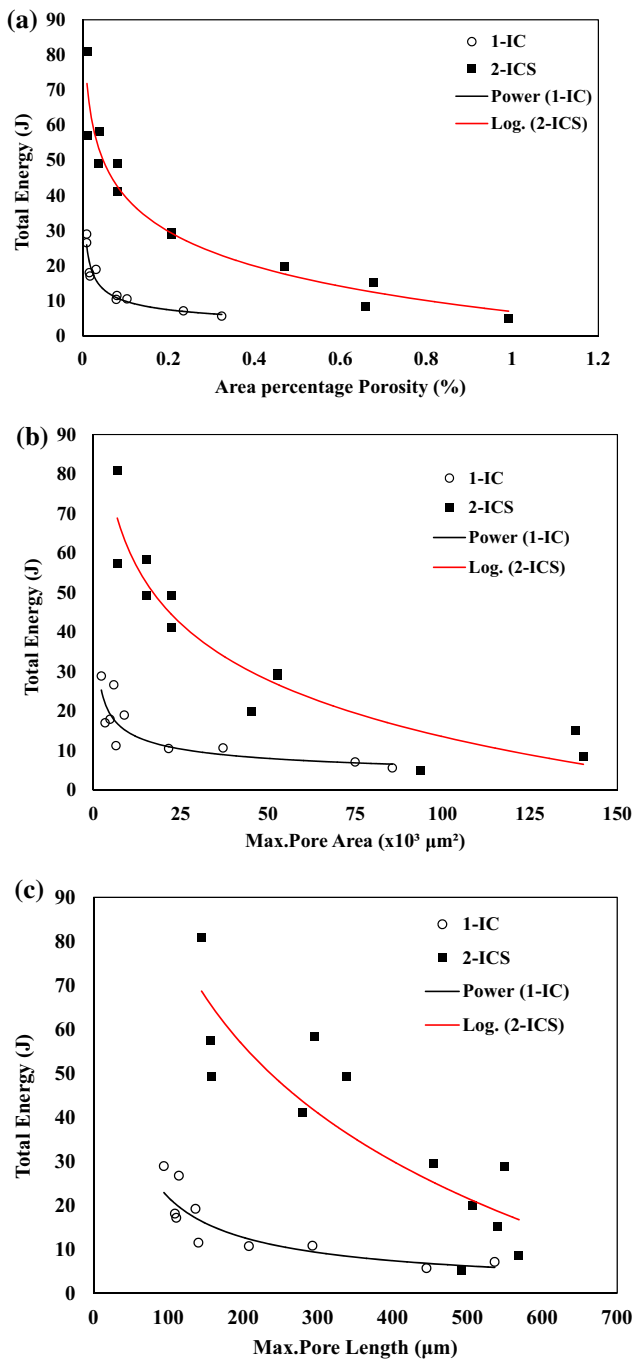
Figure 6. Total energy versus porosity parameter plots in A356.2 alloys: (a) area percentage porosity, (b) maximum pore area and (c) maximum pore length. IC = non-modified alloy, ICS = Sr-modified alloy.
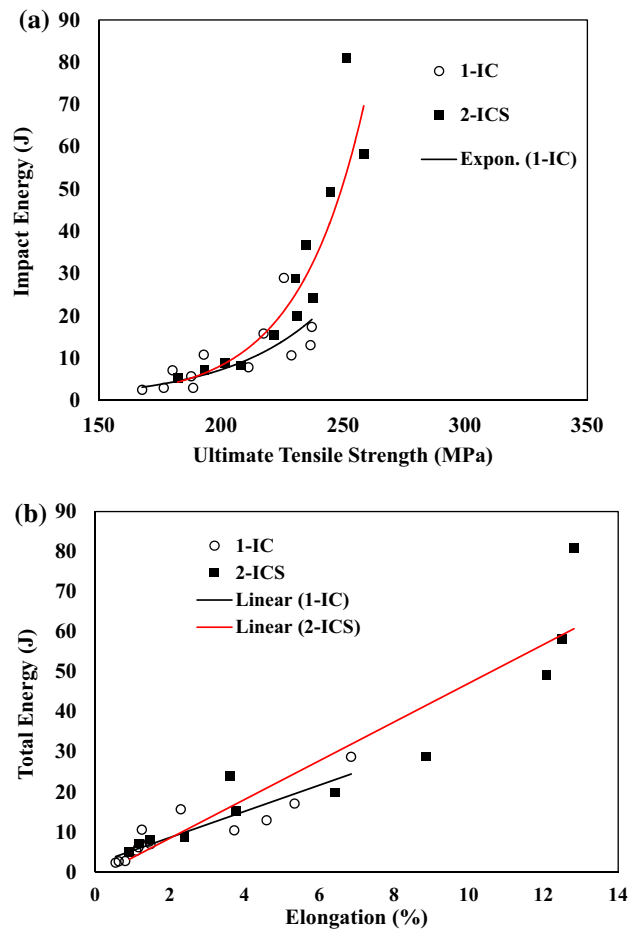

Figure 7. Correlation between impact energy and tensile properties in A356.2 alloys: (a) UTS, (b) % Elongation.

that the influence of porosity on impact test results is not very significant. The fairly good correlation between impact energy and porosity parameters obtained in our study, coupled with the correlations obtained between impact energy and β-platelet size presented in the previous sections, would appear to support the proposal that iron intermetallics facilitate the formation of porosity, as reported by other researchers.[14,16]

From Figure 6, it is evident that the 356 alloy offers high levels of toughness compared to those reported for 319 alloys, due to the absence of copper intermetallics such as $CuAl_2$, Al_7FeCu_2 and $Al_5Si_6Mg_8Cu_2$ in this alloy.[16] The addition of Sr allows for higher porosity tolerances in the alloy to maintain the same toughness levels. For example, to achieve an impact energy of ~5 J, the unmodified A356.2 alloy should contain no more than ~0.3% porosity, Figure 6a. In the modified condition, however, this level of energy can be achieved at even ~1% porosity content. The maximum pore area parameter—shown in Figure 6b—may be the appropriate parameter to characterize the overall porosity effect. Similar observations were reported for fatigue properties. The work of Lee et al.[17] on porosity control of fatigue behavior in A356-T61

shift in the curves to the left, i.e., toward smaller β-platelet sizes, narrowing the β-Al_5FeSi size range covering the reported impact energies. The rapid decrease in impact energy at smaller β-platelet sizes in the present alloys indicates that even small iron contaminations would deteriorate the impact energy considerably. Thus, in such alloys containing low levels of impurities, only small iron intermetallic sizes can be tolerated if satisfactory impact energy values are to be maintained. Tsukuda et al.[15] have observed

Iron content (%)	Sr addition	Impact energy (J)											
		DAS 23 μm (level 1)			DAS 39 μm (level 3)			DAS 53 μm (level 5)			DAS 75 μm (level 10)		
		E_I[a]	E_P[a]	E_T[a]	E_I	E_P	E_T	E_I	E_P	E_T	E_I	E_P	E_T
0.098	No	22.85	6.03	28.88	14.59	2.56	17.15	4.48	8.51	12.99	4.91	5.66	10.57
0.0936	Yes	60.44	20.44	80.88	48.86	9.31	58.17	40.06	9.13	49.19	22.60	6.20	28.80
0.429	No	5.55	10.24	15.79	5.10	5.57	10.67	5.53	1.59	7.12	4.40	1.28	5.68
0.427	Yes	33.20	3.40	36.60	14.69	5.16	19.85	7.25	7.93	15.18	6.55	2.00	8.55
0.62	No	5.63	2.13	7.76	1.31	1.66	2.97	1.08	1.81	2.89	1.14	1.31	2.45
0.605	Yes	12.48	11.56	24.04	6.34	1.71	8.05	5.12	1.86	6.98	3.41	1.46	4.87

[a] E_I, crack initiation energy; E_P, crack propagation energy; E_T, total impact energy

aluminum alloy shows that the largest pore size has the largest influence on fatigue life.

The plot of the energy data versus the corresponding maximum pore length in Figure 6c shows a large difference between Sr-modified and unmodified 356 alloys. This observation supports the above proposal that the maximum pore area is the most detrimental porosity factor affecting alloy toughness. It ought to be mentioned here that the percentage porosity and pore sizes reported for 356 alloys are much less compared to those measured for 319 alloys.[18] This difference is the result of the shorter solidification times for 356 alloys due to the absence of copper intermetallics (which precipitate in the 319 alloys). These factors attributed to the higher impact energies reported in Figure 6 for the A356.2 alloy. The effect of strontium modification on the impact energy has already been incorporated in the previous sections that discussed the effects of other parameters (i.e., iron content and solidification rate), where the unmodified alloys were compared with the modified ones. These results are discussed in the context of the figures and tables presented in the earlier sections.

For the lowest Fe-highest solidification rate sample, an improvement of 180% is noted. Table 3 shows that the improvement in impact energy of the Sr-modified alloy is not systematic with respect to the solidification rate or Fe content, as the lowest Fe samples at higher DASs (47 and 60 μm) display much higher improvements (230 and 279%, respectively). The energy is determined, rather, by how high the crack initiation energy (E_I) is for a particular sample. The E_I value primarily determines the improvement in the impact energy. The high E_I values observed in the A356.2 alloy samples reflect the effectiveness of Sr modification in this alloy which is mainly related to the eutectic Si particle characteristics. Indirectly, this observation also reveals the sensitivity of the impact properties to the alloy microstructure and to the changes therein.

The relationships between impact energy versus tensile strength and elongation are shown in Figure 7. In all cases,
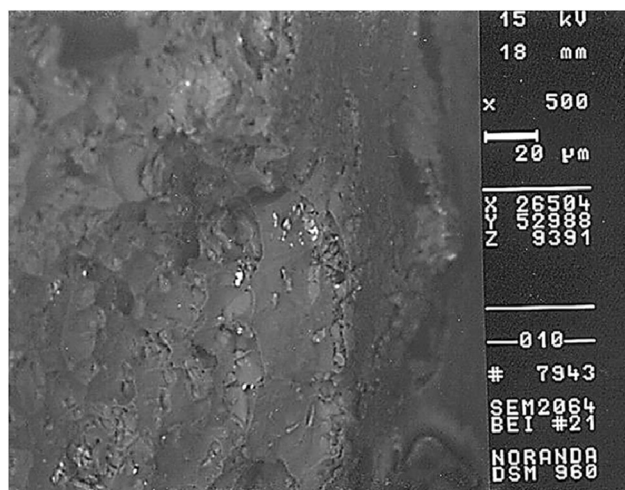

Figure 8. Backscattered electron micrograph showing fracture surface of alloy A356.2 (0.1% Fe, DAS 23 μm, modified, edge).
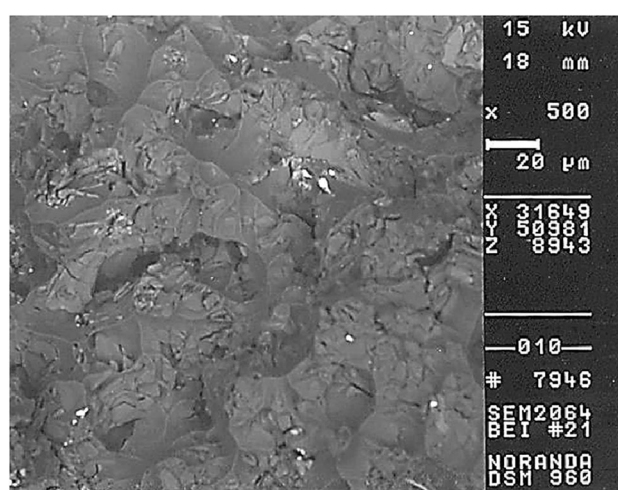

Figure 9. Backscattered electron micrograph showing fracture surface of alloy A356.2 (0.1% Fe, DAS 23 μm, modified, center).
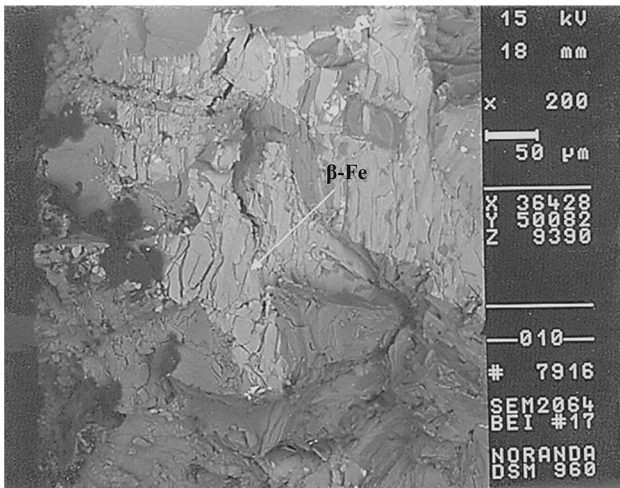
Figure 10. *Backscattered electron micrograph showing the role of β-Al$_5$FeSi intermetallics in initiating fracture in alloy A356.2 (0.6% Fe, DAS 75 μm, unmodified).*
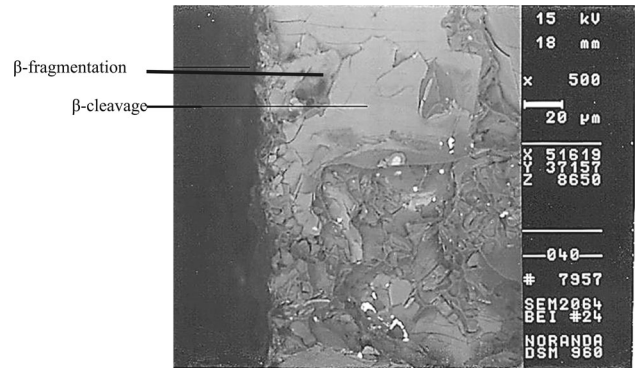

Figure 11. *(a) Backscattered electron micrograph showing crack propagation in alloy (0.6% Fe, DAS 75 μm, unmodified) and (b) EDS spectrum corresponding to β-Fe—white arrows.*

the impact energy versus tensile strength and elongation plots follow exponential and linear relationships, respectively, with the modified alloys displaying more consistent

Figure 12. *Backscattered electron micrograph showing fracture surface of alloy A356.2 (0.6% Fe, DAS 75 μm, modified, edge).*

correlations compared to the unmodified alloys. Most of the data points are distributed within impact energy ranges of 3–30 J in the 356 alloys. Figure 7a exhibits exponential correlations similar to those observed for the 319 alloys; the curves are shifted toward the left, indicating higher impact energies. The steep nature of the curve for the Sr-modified samples in Figure 7a may indicate that the effectiveness of Sr addition is both faster and greater in the A356.2 alloy.

Summarizing the results for the A356.2 alloys, it is found that the impact energy–tensile strength plots display exponential correlations, whereas the impact energy–elongation plots show linear relationships, regardless of the alloy chemical composition.

Fractography

As Voigt and Bye[19] have commented, features appearing on the fracture surfaces of Al–Si–Mg casting alloys such as A356 alloys can be very difficult to interpret due to the lack of SEM contrast between the α-Al and the eutectic Si phases appearing on the surface. As Al and Si are close in their atomic numbers, even the use of SEM techniques such as backscattered electron imaging (BEI) cannot provide additional phase contrast. However, the features observed on the fracture surfaces of the A356 alloys can be more clearly interpreted based on a study of the surface crack initiation and propagation process. Usually, by observing the microstructure just below the surface that can be observed inside the crack using SEM techniques, or else by studying longitudinal sections of the fractured samples (perpendicular to the fracture surface) using optical microscopy, additional information can be obtained that is useful in analyzing fracture behavior.

Figures 8 and 9 are the SEM fractographs taken from the modified A356.2 alloy sample containing 0.1% Fe and obtained at the highest solidification rate. Figure 8 shows the fracture to be of the transgranular dimpled rupture type. As mentioned before, the BEI image does not provide a
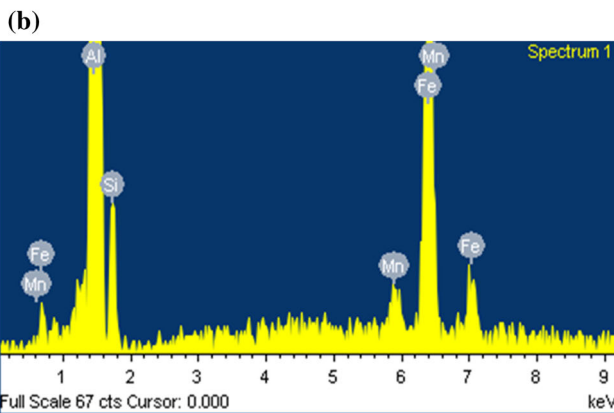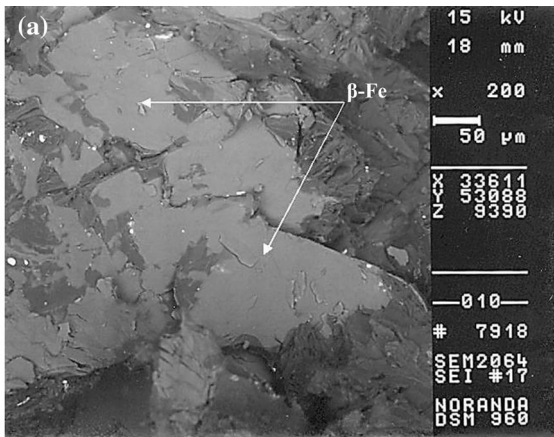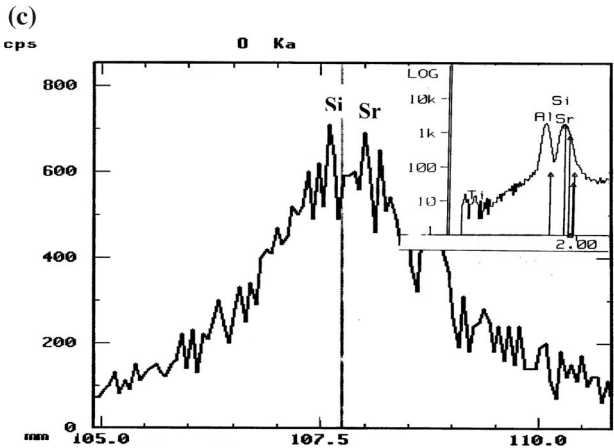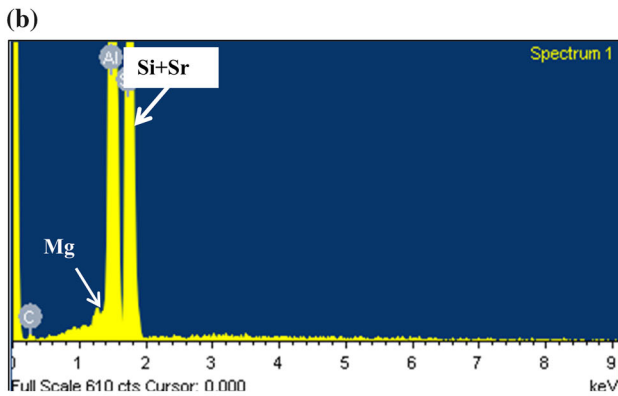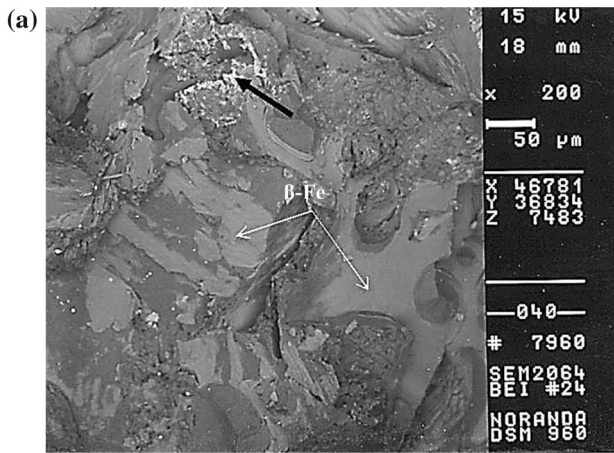
(a)

(b)

(c)

Figure 13. (a) Backscattered electron micrograph showing fracture surface of alloy (0.6% Fe, DAS 75 μm, modified, center). Note fragmentation of β-Fe—arrowed, (b) EDS spectrum obtained from the bright particles in (a)—black arrow and (c) enlargement of the Si peak showing the fusion of two peaks.[20]

Figure 14. Backscattered electron micrograph showing fracture of eutectic Si particles in alloy A356.2 (0.1% Fe, DAS 75 μm, unmodified).

Figures 10 and 11a depict the SEM fractographs of the unmodified A356.2 alloy sample containing a high Fe level (0.6%) and obtained at the lowest solidification rate. The presence of massive β-Al₅FeSi platelets in the alloy microstructure under these conditions results in the brittle fracture of the sample. Figure 10 shows that crack initiation takes place by the fragmentation of the β-phase at the edge of the sample and some amount of transgranular fracture, as well, whereas the crack propagates by cleavage fracture, as evidenced by the relatively smooth surfaces of the β-platelets observed in Figure 11a, as also by intergranular fracture. Accordingly, the impact energy of this sample was 2.45 J. The EDS spectrum shown in Figure 11b confirms that these platelets are the β-Al₅FeSi phase. When the same alloy is modified, crack initiation occurs by fragmentation of the β-platelets, followed by cleavage, as shown in Figure 12. Modified silicon eutectic regions around the β-platelet can also be distinguished. Figure 13a reveals a mixture of cleavage and intergranular fracture, while the presence of Sr is confirmed by Figure 13b, c.[20]

The high-magnification SEM fractograph of an unmodified A356.2 alloy sample containing 0.1% Fe and obtained at the lowest solidification rate, Figure 14, reveals the eutectic Si regions much more clearly, where the fracture is seen to occur by transgranular mode, by the brittle fracture of the acicular Si particles (circled areas). Regardless of SEM fractography, it is also quite useful to examine the fracture profile on sections perpendicular to the fracture surface. This can be carried out easily using an optical microscope. In this way, the origin of the fracture can be examined to determine whether important microstructural abnormalities are present that either caused or contributed to fracture initiation. It is also possible to determine whether the fracture path at the initiation site is transgranular or intergranular and to determine whether the fracture path is

good phase contrast. The fractograph of Figure 9, taken from the center of the sample, shows these features more clearly. Note the fine Si particles in the structure. The absence of intermetallics due to the low Fe content, together with the fine Si particles obtained under the high solidification rate and Sr modification, results in the sample exhibiting the highest impact energy (80.88 J).
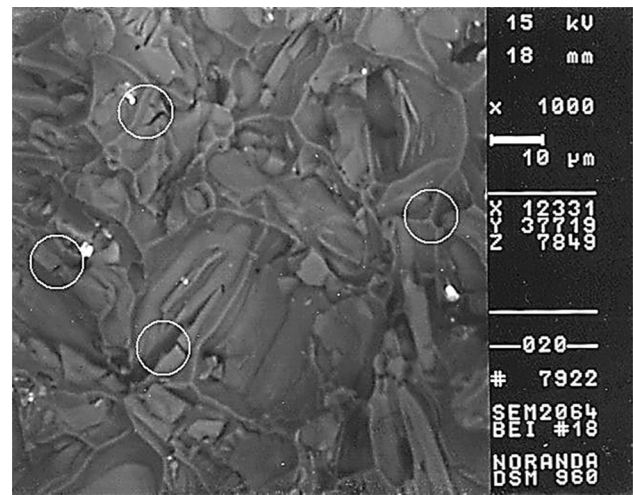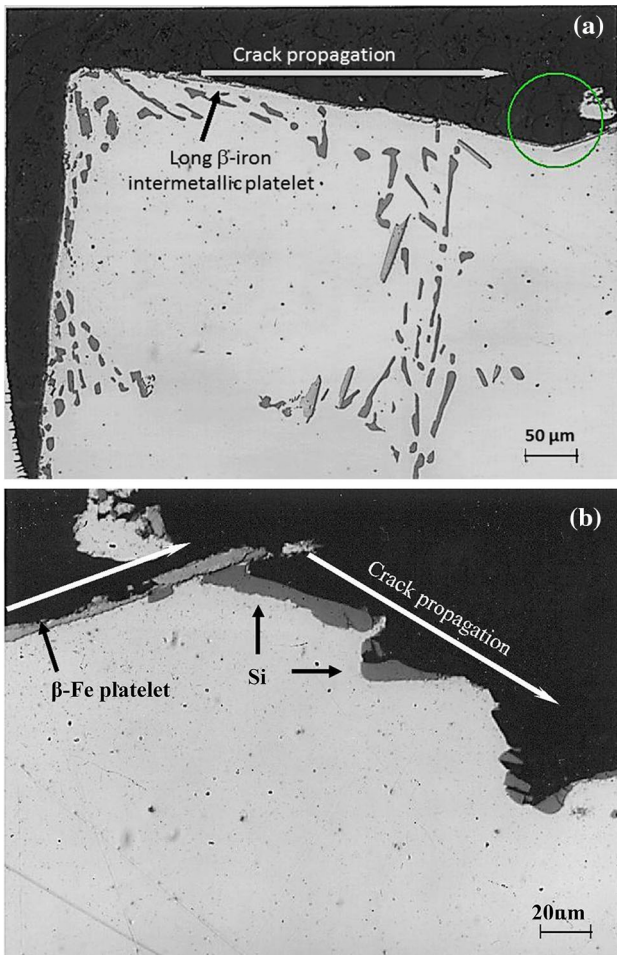
774

Figure 15. Optical microstructures showing fracture behavior of alloy A356.2 (0.6% Fe, DAS 75 μm, unmodified, edge). A high-magnification micrograph of areas similar to those in the circled area in (a) is shown in (b).

Figure 16. Optical micrographs showing fracture behavior of alloy A356.2 (0.1% Fe, DAS 23 μm, Sr-modified, edge).

specific to any phase or constituent present.[21] Some examples of the longitudinal sections of the A356.2 alloy samples are presented in this section with a view to further clarifying the fracture process in these samples since their SEM fractographs did not provide a good contrast.

The optical micrographs presented in Figure 15 show the polished longitudinal section of the fractured A356.2 unmodified alloy sample containing 0.6% Fe, obtained at the lowest solidification rate. In (a), the edge of the sample on the left shows how crack initiation occurs by the cleavage and/or transgranular fracture of the Si particles and β-Al5FeSi platelets. The sample edge corner is relatively straight, indicating that cracking occurred almost immediately, i.e., by brittle fracture mode, and the crack propagated along the direction shown. The higher-magnification micrograph in Figure 15b, taken from an area similar to that circled in (a), shows how the crack propagates further along the fracture surface by cleavage of the β-iron intermetallic and coarse Si particles. The persistence of such coarse Si particles, even after solution heat
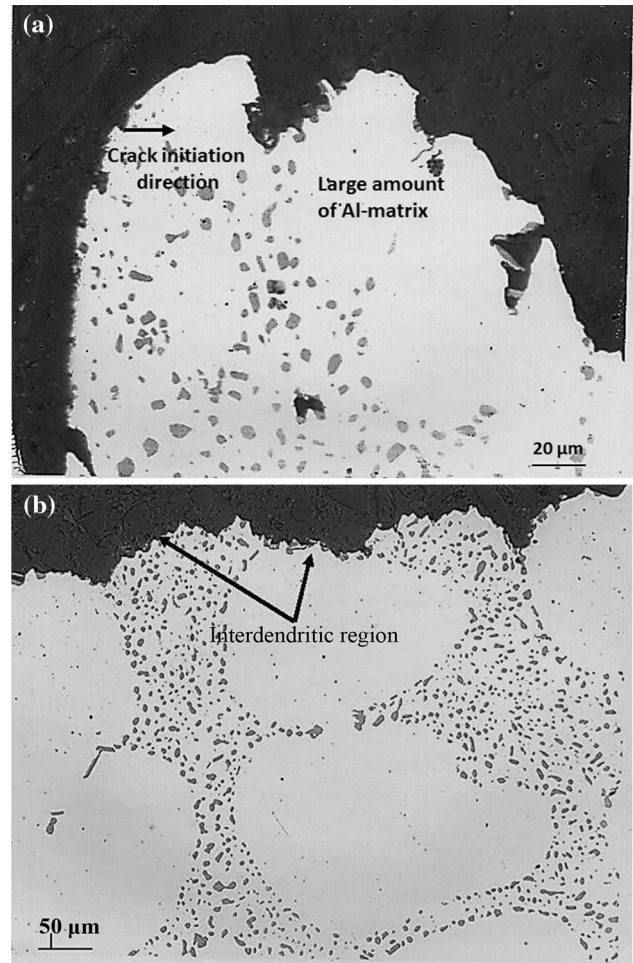
treatment at 540 °C/8 h, aids in inducing the brittle fracture of the sample. Correspondingly, under such alloy conditions, the sample exhibited the lowest impact energy, i.e., 2.45 J (see Table 3). Figure 15 provides a good example of how optical microscopy can aid in providing a clearer interpretation of the crack initiation and propagation in A356 type Al–Si–Mg alloys.

Compared to the micrographs shown in Figure 15 those obtained from the A356.2 alloy sample corresponding to optimum energy conditions (viz. 0.1% Fe, lowest solidification rate, modified alloy), Figure 16a shows how the sample edge is more curved or rounded rather than flat as was observed in the case of the unmodified alloy sample of Figure 15a. The curvature of the fracture surface, also clearly observed in Figure 16b, indicates a ductile mode of rupture as the crack propagates through the well-modified Si eutectic regions. The E_I, E_P and E_T in this case are of 60.44, 20.44 and 80.88 J, respectively, compared to those of 1.41, 1.31 and 2.45 J in the case of the sample shown in Figure 15.
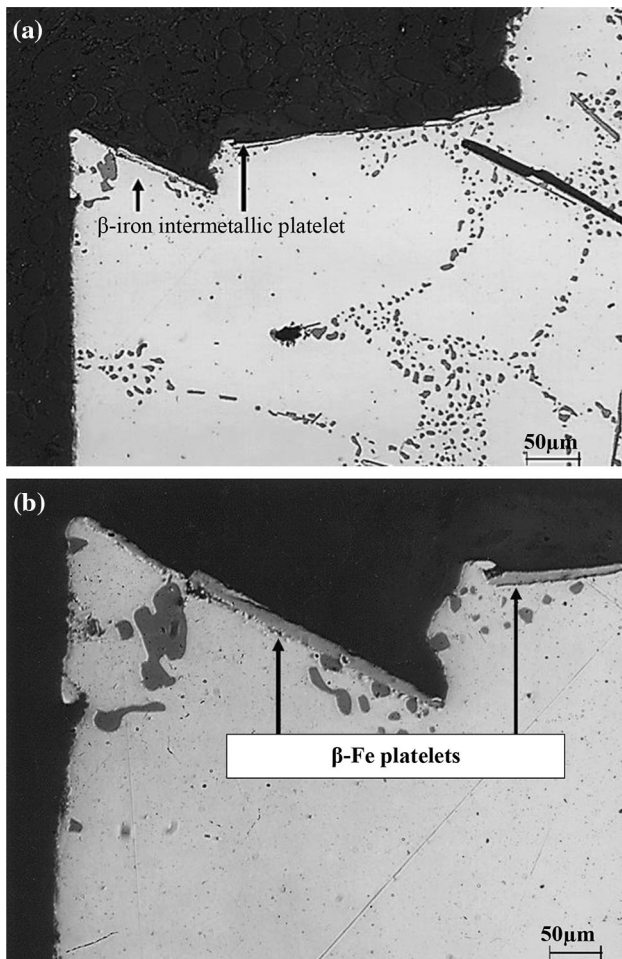
Figure 17. *Optical micrographs showing fracture behavior of alloy A356.2 (0.6% Fe, DAS 75 μm, Sr-modified, edge).*

However, when the alloy Fe level is increased and the solidification rate decreased to its lowest value, even in the Sr-modified alloy, the fracture still occurs mainly by cleavage of the brittle β-Al₅FeSi platelets, Figure 17a. Note the sharp edge of the sample fracture surface in this case, compared to Figure 16. Figure 17b shows these features much more clearly at high magnification. In instances when the crack propagates through the more ductile Al–Si regions, the fracture surface is more rounded than sharp. The corresponding E_I, E_P and E_T are 3.41, 1.46 and 4.87 J, respectively.

Conclusions

The present research study was carried out to investigate the effect of iron intermetallics and porosity on the performance of Al–Si–Mg (356) cast alloys, using castings obtained under directional solidification conditions, and subjected thereafter to T6 heat treatment. From an analysis of the results obtained, the following may be concluded.

1. Logarithmic correlations are obtained at all solidification rates in modified A356.2 alloys. In all cases, the correlations are quite good, with $R^2 > 0.95$.

2. The highest solidification rate provides impact energies far superior to those obtained at other solidification rates (e.g., 12.40 J at 23 μm DAS compared to 4.88 J at 85 μm DAS in the unmodified 319.2 alloy at 0.4% Fe level, and 30.96 J vs. to 11.35 J in the Sr-modified case).

3. The presence of the β-Al₅FeSi phase deteriorates the impact properties significantly. The effect is most apparent for β-platelet lengths within the range of 10–50 μm in the A356.2 alloy, as illustrated by the power correlations between impact energy and β-platelet length/area obtained in all the alloys (with $R^2 > 0.95$).

4. Strontium modification is effective in improving the impact energy, even at high iron levels. In the case of the A356.2 alloy, the improvement rates at the lowest (0.1%) and highest (0.6%) iron contents are higher than that at moderate iron content (0.4%).

5. The average crack speed of impact-tested samples shows a good inverse relation with impact energy: the highest crack speeds are normally obtained for the unmodified samples corresponding to the highest iron contents and lowest solidification rates.

6. Impact testing is more sensitive to variations in microstructure or casting defects than tensile testing. The impact energy–ultimate tensile strength plots display exponential relationships, while the impact energy–percentage elongation plots display linear relationships in both unmodified and Sr-modified alloys, regardless of alloy composition.

7. In the A356.2 alloys, in samples obtained under optimum conditions (0.1% Fe, 23 μm DAS, Sr-modified), cracks initiate mainly through the fracture of Si particles or the debonding of the Si particles from the Al matrix.

8. In the unmodified condition, cracks mainly propagate through the coalescence of fractured Si particles, except where β-iron intermetallics are present, in which case the latter takes priority in fracture propagation.

9. In the Sr-modified condition, more of the Al matrix is involved when cracks propagate through the linkage of fractured/debonded Si particles, as well as fragmented β-iron intermetallics. For samples characterized by low impact energies, crack initiation and propagation occurs mainly through the cleavage of β-iron intermetallics.

REFERENCES

1. Z. Ma, A.M. Samuel, F.H. Samuel, H.W. Doty, S. Valtierra, Effect of iron and cooling rate on tensile properties of B319.2 alloys in non-modified and Sr-modified conditions. AFS Trans. **112**, 131–140 (2004)
2. B. Golbahar, A.M. Samuel, F.H. Samuel, H.W. Doty, S. Valtierra, Effect of grain refiner–modifier interaction on the microstructure and mechanical properties of A356.2 alloys. AFS Trans. **115**, 1–13 (2007)
3. J.A. Taylor, Iron-containing intermetallic phases in Al–Si based casting alloys. Proc. Mater. Sci. **1**, 19–33 (2012)
4. L.A. Narayanan, F.H. Samuel, J.E. Gruzleski, Dissolution of iron intermetallics in Al–Si alloys through nonequilibrium heat treatment. Metall. Mater. Trans. A **26**, 2161–2174 (1995)
5. Z. Ma, A.M. Samuel, F.H. Samuel, H.W. Doty, Effect of Fe content and cooling rate on the impact toughness of cast 319 and 356 aluminum alloys, in *Transactions of the American Foundry Society: volume 111; 107th casting congress April 26–29, 2003* (American Foundry Society, 2003), pp. 255–265
6. S. Ji, W. Yang, F. Gao, D. Watson, Z. Fan, Effect of iron on the microstructure and mechanical property of Al–Mg–Si–Mn and Al–Mg–Si diecast alloys. Mater. Sci. Eng. A **564**, 130–139 (2013)
7. Y. Komiyama, K. Uchida, M. Gunshi, Effect of Fe, Mn, Zn and Ti on mechanical properties and microstructures of Al–Si–Cu–Mg casting alloy. J. Jpn. Inst. Light Met. **26**, 311–319 (1976). **(in Japanese)**
8. Z. Ma, E. Samuel, A.M.A. Mohamed, A.M. Samuel, F.H. Samuel, H.W. Doty, Parameters controlling the microstructure of Al–11Si–2.5Cu–Mg alloys. Mater. Des. **31**, 902–912 (2010)
9. S. Nishi, T. Kobayashi, A study on the toughness of aluminum alloy castings. J. Jpn. Foundrymen's Soc. **46**, 905–912 (1974). **(in Japanese)**
10. M.A. Moustafa, F.H. Samuel, H.W. Doty, Effect of solution heat treatment and additives on the hardness, tensile properties and fracture behaviour of Al–Si (A413.1) automotive alloys. J. Mater. Sci. **38**, 4523–4534 (2003)
11. M.F. Hafiz, T. Kobayashi, N. Fat-Halla, Tensile properties influencing variables in eutectic Al–Si casting alloys. Scr. Metall. Mater. **31**, 701–705 (1994)
12. M.D. Dighe, A.M. Gokhale, Relationship between microstructural extremum and fracture path in a cast Al–Si–Mg alloy. Scr. Mater. **37**, 1435–1440 (1997)
13. M.F. Ibrahim, A.M. Samuel, H.W. Doty, F.H. Samuel, Effect of aging conditions on precipitation hardening in Al–Si–Mg and Al–Si–Cu–Mg alloys. Int. J. Metalcasting (2016). doi:10.1007/s40962-016-0057-z
14. M.F. Ibrahim, E. Samuel, A.M. Samuel, A.M.A. Al-Ahmari, F.H. Samuel, Impact toughness and fractography of Al–Si–Cu–Mg base alloys. Mater. Des. **32**, 3900–3910 (2011)
15. H.W. Doty, S.A. Alkahtani, O. Elsebaie, F.H. Samuel, Influence of metallurgical parameters on the impact toughness of near eutectic Al–Si alloys, in *119th Metalcasting Congress, AFS 2015, Columbus, OH, April 21–23, 2015* (American Foundry Society, Columbus, 2015)
16. K.A. Abuhasel, M.F. Ibrahim, E.M. Elgallad, F.H. Samuel, On the impact toughness of Al–Si cast alloys. Mater. Des. **91**, 388–397 (2016)
17. F.T. Lee, J.F. Major, F.H. Samuel, Effect of silicon particles on the fatigue crack growth characteristics of Al–12 wt% Si–0.35 wt% Mg–(0 to 0.02) Wt% Sr casting alloys. Metall. Mater. Trans. A **26**, 1553–1570 (1995)
18. L. Liu, Metallurgical parameters controlling the microstructural evolution of Al-Si-Mg and Al-Si-Cu alloys, PhD Thesis, Université du Québec à Chicoutimi, Québec, Canada, 2004
19. R.C. Voigt, D.R. Bye, Microstructural aspects of fracture in A356. AFS Trans. **99**, 33–50 (1991)
20. A.M. Samuel, H.W. Doty, S. Valtierra, F.H. Samuel, Influence of oxides on porosity formation in Sr-treated alloys. Int. J. Metal Casting (2016). doi: 10.1007/s40962-016-0118-3
21. O. Vorren, J.E. Evensen, T.B. Pedersen, Microstructure and mechanical properties of AlSi(Mg) casting alloys. AFS Trans. **92**, 459–466 (1984)